UCSF
UC San Francisco Previously Published Works

Title
Optimization of an endovascular magnetic filter for maximized capture of magnetic nanoparticles

Permalink
https://escholarship.org/uc/item/0pm6h025

Journal
Biomedical Microdevices, 18(6)

ISSN
1387-2176

Authors
Kondapavulur, Sravani
Cote, Andre M
Neumann, Kiel D
et al.

Publication Date
2016-12-01

DOI
10.1007/s10544-016-0135-2

Peer reviewed

eScholarship.org Powered by the California Digital Library
University of California

Author Manuscript

Author Manuscript

Author Manuscript

Author Manuscript

HHS Public Access

Author manuscript

Biomed Microdevices. Author manuscript; available in PMC 2017 December 01.

Published in final edited form as:

Biomed Microdevices. 2016 December ; 18(6): 109. doi:10.1007/s10544-016-0135-2.

Optimization of an endovascular magnetic filter for maximized capture of magnetic nanoparticles

Sravani Kondapavulur[1,2], **Andre M. Cote**[1], **Kiel D. Neumann**[1], **Caroline D. Jordan**[1], **David McCoy**[1], **Marc C. Mabray**[1], **Derek Liu**[2], **Chia-Hung Sze**[1], **Ayushi Gautam**[1], **Henry F. VanBrocklin**[1], **Mark Wilson**[1], and **Steven W. Hetts**[1]

[1]Department of Radiology and Biomedical Imaging, University of California, 505 Parnassus Avenue, L-351, San Francisco, CA 94143-0628, USA

[2]Department of Bioengineering, University of California, Berkeley, CA, USA

Abstract

To computationally optimize the design of an endovascular magnetic filtration device that binds iron oxide nanoparticles and to validate simulations with experimental results of prototype devices in physiologic flow testing. Three-dimensional computational models of different endovascular magnetic filter devices assessed magnetic particle capture. We simulated a series of cylindrical neodymium N52 magnets and capture of 1500 iron oxide nanoparticles infused in a simulated 14 mm-diameter vessel. Device parameters varied included: magnetization orientation (across the diameter, “D”, along the length, “L”, of the filter), magnet outer diameter (3, 4, 5 mm), magnet length (5, 10 mm), and spacing between magnets (1, 3 mm). Top designs were tested *in vitro* using ^{89}Zr-radiolabeled iron oxide nanoparticles and gamma counting both in continuous and multiple pass flow model. Computationally, “D” magnetized devices had greater capture than “L” magnetized devices. Increasing outer diameter of magnets increased particle capture as follows: “D” designs, 3 mm: 12.8–13.6 %, 4 mm: 16.6–17.6 %, 5 mm: 21.8–24.6 %; “L” designs, 3 mm: 5.6–10 %, 4 mm: 9.4–15.8 %, 5 mm: 14.8–21.2 %. *In vitro*, while there was significant capture by all device designs, with most capturing 87–93 % within the first two minutes, compared to control non-magnetic devices, there was no significant difference in particle capture with the parameters varied. The computational study predicts that endovascular magnetic filters demonstrate maximum particle capture with “D” magnetization. *In vitro* flow testing demonstrated no difference in capture with varied parameters. Clinically, “D” magnetized devices would be most practical, sized as large as possible without causing intravascular flow obstruction.

Keywords

Intra-arterial chemotherapy (IAC); Magnetic nanoparticles; Chemofiltration; Endovascular device

Correspondence to: Steven W. Hetts.

Author Manuscript Author Manuscript Author Manuscript Author Manuscript

1 Introduction

Several groups have explored how to remove chemotherapy from the blood using technologies such as extracorporeal filtration and endovascular ionic resin-based filtration (Fuhrman et al. 1994; Curley et al. 1993, 1994; Song et al. 2012; Lammer et al. 2010; Patel et al. 2014). More recently, an endovascular magnetic filter has been developed to remove ferromagnetic nanoparticle-conjugated chemotherapy from the blood, thereby minimizing systemic toxicity and allowing for higher dose therapy (Mabray et al. 2015), as seen in Fig. 1a. Previously, this device demonstrated rapid binding of iron oxide nanoparticles *in vitro* in swine serum. In this study, we aim to computationally optimize a magnetic endovascular filtration device that binds iron oxide nano-particles through finite element modeling, and to validate the simulated results with experimental results of prototype devices in *in vitro* physiologic flow.

Chemotherapeutic agents, such as doxorubicin, can be conjugated to magnetic nanoparticles and microparticles for use in intra-arterial chemotherapy (IAC), particularly when combined with an external magnetic field to direct movement of therapy into target tissue (El-Sayed 2010; Lyer et al. 2010; Wilson et al. 2004; Goodwin et al. 2001). Doxorubicin conjugated to 1.4 micron magnetically-targeted carrier particles (MTC-DOX), for example, has been used for magnetic drug targeting in patients with hepatocellular carcinoma (Wilson et al. 2004; Goodwin et al. 2001). However, even with local targeting much of the therapy can continue downstream into systemic circulation, causing dose-limiting side effects.

Within the field of magnetic drug targeting, many groups have computationally modeled ferromagnetic fluid paths and magnetic particle trajectories with the application of an external magnetic field (Mahmoudi et al. 2009; Cao et al. 2012; Driscoll et al. 1984; Haverkort et al. 2009; Furlani and Ng 2006; Ratariu and Strachan 2005; Sharma et al. 2015). These multiphysics principles, including magnetism, laminar flow, fluid-particle interactions, and more, can be utilized to explore the interaction of our device with the surrounding fluid and particles within it. Specifically, we can build on these simulations to examine magnetic fields generated by the device, laminar flow around the device, and how physical properties of iron oxide nanoparticles affect interaction with the fluid and our device.

By varying physical parameters of the magnetic device to maximize theoretical particle capture, and additionally prototyping and testing these devices *in vitro*, we can build a device that can minimize systemic toxicity of therapy and enable higher dosing. We hypothesize that magnetic devices that demonstrated greater theoretical capture of particles would similarly capture iron oxide particles *in vitro*. The purpose of this study was to optimize the design parameters of an intravascular magnetic filter to capture iron oxide nanoparticles in a flow model.

Author Manuscript Author Manuscript Author Manuscript Author Manuscript

2 Materials and methods

2.1 Device design

To create the integrated device particle capture simulation, simplified geometries of a given device were built within the COMSOL application (COMSOL Multiphysics Version 5.1, Stockholm, Sweden). Four solid cylinders were built in series along the z-axis with 3, 4, or 5 mm diameters and 1 or 3 mm spacing between magnets, and 5 mm length (Fig. 1). For devices with 10 mm individual magnet length, 2 cylinder magnets were simulated with 3, 4, or 5 mm diameters and 1 or 3 mm spacing. These cylinders were assigned the physical properties of iron, and a relative permeability $\mu_r = 1.05$. Finally, each design had magnets with magnetization along the length of the cylinder in alternating orientation ("L" devices) or across the diameter in alternating orientation ("D" devices). Device geometries that were computationally evaluated are summarized in Table 1.

2.2 Magnetic field simulation

In order to generate the magnetic field simulation, a sphere of air (radius = 100 mm, $\mu_r = 1$) was built as an environment around the magnets, and by Maxwell-Ampere's law of magnetic flux conservation, the boundary domain was defined to have no current

$$\mathbf{H} = -\nabla V_m, \quad (1)$$

where **H** is the magnetic field strength, V_m is the magnetic scalar potential, and μ_0 is the physical constant of vacuum permeability. In combination with Gauss's law for magnetism,

$$\nabla \cdot \mathbf{B} = 0, \quad (2)$$

where **B** is the magnetic flux density on this spherical surface, the equation can be rearranged such that

$$\nabla \cdot (\mu_0 \mu_r \mathbf{H}) = 0. \quad (3)$$

Additionally, magnetic insulation was defined on a point on this sphere by the following stationary equation:

$$\mathbf{n} \cdot \mathbf{B} = 0 \quad (4)$$

where **n** is a unit normal at the boundary surface. Finally, all geometric domains in the simulation were initially assigned $V_m = 0A$.

Author Manuscript Author Manuscript Author Manuscript Author Manuscript

The cylinder geometries were then assigned magnetic properties consistent with neodymium-52 permanent magnets (remanent flux density of 14.5 KGs/1.45 T; K&J Magnetics, Pipersville, Pennsylvania), characterized by the remanent flux density constitutive relation

$$\mathbf{B}=\mu_0\mu_\mathrm{r}\mathbf{H}+\mathbf{B_r}, \quad (5)$$

where **B** is the resultant magnetic flux density of the system, $\mathbf{B_r}$ is the assigned remanent flux density for each cylinder, and μ_r is the relative permeability of the cylinder. For devices that had alternating magnetization across the diameter, the first and third magnets had $\mathbf{B_r}$ (1.45,0,0) [T], while the second and fourth magnets had $\mathbf{B_r}$ (−1.45,0,0) [T]. Devices that had alternating magnetization across the length (along the z-axis) had $\mathbf{B_r}$ (0,0,1.45) [T] for the first (and third) magnets and $\mathbf{B_r}$ (0,0,−1.45) [T] for the second (and fourth) magnets.

2.3 Laminar flow simulation

A simplified vessel flow simulation was generated in COMSOL by constructing a larger cylinder centered around the magnets with a radius = 7 mm, and length = 100 mm. Material properties were assumed to be those of water: dynamic viscosity, μ, was defined as η (T[1/K])[Pa*s], where η was the dynamic viscosity of water as given by COMSOL materials library; density, ρ, as rho(T[1/K])[kg/m^3], where rho was the density of water as given by the COMSOL materials library; relative permeability, μ_r, as 1; and temperature, T, as 293.15 K. The model assumed steady state, incompressible laminar flow, and thus a stationary solution could be reached with the following Navier–Stokes equation

$$\rho(\mathbf{u}2\cdot\nabla)\mathbf{u}2=\nabla\cdot\left\{-p2\mathbf{I}+\mu\left[\nabla\mathbf{u}2+(\nabla\mathbf{u}2)^{\mathrm{T}}\right]\right\}+\mathbf{F} \quad (6)$$

along with the continuity equation

$$\rho\nabla\cdot(\mathbf{u}2)=0 \quad (7)$$

where **u2** is the velocity field through the cylinder, $p2$ is the pressure along the cylinder, **I** is the identity matrix, and **F** corresponds to external forces applied to the fluid. The initial value of the velocity field was set to be (0,0,0.1) m/s (Wexler et al. 1968) with zero pressure gradient along the vessel. Additionally, a no-slip boundary condition was set at the outer wall.

An inlet boundary condition was defined by the stationary equation

$$\mathbf{u}2=-U_0\mathbf{n}, \quad (8)$$

Author Manuscript Author Manuscript Author Manuscript Author Manuscript

where U_0 is the normal inflow velocity, defined to be 0.1 m/s and the outlet boundary condition by equation the following relationship

$$\left\{-\rho 2\mathbf{I}+\mu\left[\nabla\mathbf{u}2+(\nabla\mathbf{u}2)^{\mathbf{T}}\right]\right\}\mathbf{n}=-\hat{p}_0\mathbf{n},\hat{p}_0\leq p_0 \quad (9)$$

where $\hat{p}_0$ is the unit vector of the pressure condition (p_0), defined to be 0 Pa.

To solve both the magnetic field and laminar flow simulations, a physics-controlled mesh of fine element size was built across all of the simulation domains: magnet cylinders, flow cylinder, and environmental air sphere. A stationary study then simultaneously solved for the magnetic field generated and flow around the device for each case.

2.4 Particle tracing simulation

We simulated the capture of 1500 iron oxide microparticles by each device. Particle density, ρ_p, was set to 5240 [kg/m^3] (Guskos et al. 2010), and the diameter of each particle, d_p, was 1.0 μm. A drag force (**F**) was assigned to the particles

$$\mathbf{F}=m_{\mathrm{p}}(\mathbf{u}-\mathbf{v})/\mathrm{T_p} \quad (10)$$

where the input velocity field, **u**, was derived from the laminar flow solution, m_{p} is the calculated mass of each particle, and τ_{p} is the shear stress on the surface of the particle, as described below.

$$\mathrm{T_p}=\rho_p {d_p}^2/18\,\mu \quad (11)$$

The particles were also given an external magnetophoretic force ($\mathbf{F_t}$), as seen below,

$$\mathbf{F_t}=2\,\pi\,{r_p}^3\,\mu_0\,\mu_r K\nabla\mathbf{H}^2 \quad (12)$$

where the input magnetic field (**H**) was derived from the device magnetic field solution, particle relative permeability, $\mu_{\mathrm{r,p}}$, was 4000 (Brown 1958), r_p was the radius of each particle, and K was a constant for this system as detailed below.

$$K=(\mu_{\mathrm{r,p}}-\mu_{\mathrm{r}})\,/\,(\mu_{\mathrm{r,p}}+2\mu_{\mathrm{r}}) \quad (13)$$

A primary wall condition was set for the vessel cylinder such that particle velocity was adjusted (from $\mathbf{v_c}$ to **v**) upon bouncing off of the wall

Author Manuscript Author Manuscript Author Manuscript Author Manuscript

$$\mathbf{v}=\mathbf{v_c}-2(\mathbf{n}\cdot\mathbf{v_c})\mathbf{n}. \quad (14)$$

For the magnets, a secondary wall condition was set such that any particle encountering the surface would remain at the site of contact. We then simulated the release of 500 particles at times 0, 0.2, and 0.4 s, with initial velocity of the particles being the flow velocity of the liquid. At the outlet, a freeze-wall condition was applied to validate that particles either remained on the surface of the magnet or flowed past to the outlet. A time-dependent study then implemented the previous magnetic field and laminar flow stationary solutions to solve for the particle tracing solution.

2.5 Magnetic devices

Prototype devices of different outer diameters (OD), lengths, spacing between magnets, and magnetization orientations were constructed for *in vitro* physiologic flow testing, as summarized in Table 2. All devices were constructed from neodymium N52 grade, 1 mm inner diameter ring magnets (SuperMagnetMan Magnetics, Pelham, Alabama). Magnets with polarization along the length were strung along a 0.018 in/0.46 mm diameter clinical endovascular Terumo Glidewire GT guide wire (Boston Scientific, Natick, MA) with same polarities facing each other and secured with metal crimp tubes on either end. Magnets with polarization across the diameter were strung onto the guide wire with opposite polarities facing each other. Spacing between the individual magnets was achieved by placing rubber spacers along the guide wire between the magnets (rubber/plastic blend, 1/32″ inner diameter, 5/32″ outer diameter, 1/16″ wall thickness; McMaster Carr), and metal crimp tubes were placed on either end of the magnets to prevent sliding. In both cases, either 14 magnets of 5 mm length or 7 magnets of 10 mm length comprised a single device (Fig. 2a).

Additionally, non-magnetic (“sham”) metallic devices were built as controls. To simulate devices with magnetization across the diameter (“D” devices), non-magnetic hematite beads (4.5 mm outer diameter, 6.0 mm length) were strung onto the guide wire with the same 1 mm rubber tubing spacers in between and metal ring clamps on either end of the device. To simulate devices with magnetization across the length (“L” devices), non-magnetic hematite beads with the same dimensions were superglued to the guide wire to constrain spacing to 1 mm; metal ring clamps were placed on either side of the device. All prototype devices built for *in vitro* flow testing are summarized in Table 2.

2.6 Radiolabeled quantification

A 4 mL (1 dram) vial was charged with 250 mg of iron oxide nanoparticles, which were then suspended in 300 μL of Omni water. Next, 100 μCi of ^{89}Zr-zirconium chloride in 1 M oxalic acid (3D Imaging, Little Rock, AR), was added to the suspension and neutralized to pH 7 with the appropriate volume of 2 M sodium carbonate. The suspension was briefly mixed by shaking and then placed in an aluminum block heater at 120 °C for 2 h. The vial was removed and cooled to room temperature. The nanoparticles were then concentrated to the bottom of the vial using three large cylindrical N52 magnets connected in series, and the

Author Manuscript Author Manuscript Author Manuscript Author Manuscript

water was decanted; this process was repeated twice more. The labeling yield was quantitative and ^{89}Zr-Fe_3O_4 nanoparticles were used without any further purification.

2.7 *In vitro* flow modeling

In vitro quantification of device design performance was evaluated using a bench-top flow model system that mimics a simulated inferior vena cava vascular blood flow. Several prototype devices were tested with a continuous flow phosphate buffered saline (PBS) solution setup for initial evaluation. To test further physiological constraints of the system and provide more rigorous testing, 3 and 4 mm OD devices were tested in a multiple pass flow setup with porcine serum solution to more closely replicate blood medium (Tables 3 and 4).

A bench top flow model was constructed using 1.2 cm inner diameter flexible polyvinylchloride tubing (Masterflex, Vernon Hills, Illinois), connected to either one or two fluid reservoirs depending on continuous or multiple pass experimental setup, and was propelled at a rate of 750 mL/min by a peristaltic pump (Masterflex). Approximately 15 cm distal to the pump, one of the magnetic or dummy collection devices was suspended *via* wire within the lumen of the tubing as flow passed around it. In each experiment 500 mL of either PBS or porcine serum was combined with 250 mg of 50–100 nm ^{89}Zr-Fe_3O_4 [0.5 g/L] and passed through the tubing.

2.8 Continuous flow

For each magnetic or non-magnetic device, an experimental and control continuous flow trial was performed, with control trials performed without the device inserted into the tubing and experimental trials using the device. Continuous flow experiments utilized a single 1 L reservoir connected to both ends of the flow model tubing, containing the 500 mL PBS solution (Fig. 2b). After an initial 3 mL sample of the solution was taken, the flow model was then allowed to run for 10 min. In control experiments, three subsequent 3 mL solution samples were taken at the 1, 5, and 10 min time points during the 10 min of flow and averaged for subsequent normalization. In the experimental group trials, four additional 3 mL samples were collected at the 0.5, 1, 2, 5, and 10 min time points. The control and experimental trial process was then repeated two additional times using new devices, for a total of three control and three experimental trials for each magnetic or non-magnetic device.

2.9 Multiple pass

Multiple pass trials, performed to simulate the ability of devices to capture particles on the first pass and subsequent passes through the vena cava in patients, utilized two individual 1 L reservoirs, with one containing the original 500 mL serum solution at the start, and one to collect the solution as it passed through the model (Fig. 2d). During approximately 60 s of flow, the entirety of the 500 mL solution was passed from the first reservoir, across the device within the tubing, into the second reservoir. This constituted a single pass through our flow model system. This was repeated twice, for each device, by recovering the solution from the second reservoir and returning it to the first reservoir. For all multiple pass trials, an initial 3 mL solution sample was obtained prior to activation of flow and again after each

Author Manuscript Author Manuscript Author Manuscript Author Manuscript

completion of flow from the first to second reservoir. Subsequently, for each device and dummy device, we obtained a 1, 2, and 3 total pass 3 mL solution sample.

2.10 Quantification – gamma counting

Gamma counting was used to assess solution sample $^{89}Zr\text{-}Fe_3O_4$ concentration. Solution aliquots, 3 mL, were placed into an automated gamma counter (Wallac Wizard 3, Perkin Elmer) to quantify ^{89}Zr activity over a 1 min count time.

2.11 Quantification – 2 dimensional imaging

Devices were imaged using an AR-2000 (Bioscan, Washington DC) linear imager. Devices were placed within thin protective plastic sheaths and aligned longitudinally with the detector arm. Individual photon emissions were recorded along the length of the device with millimeter spatial resolution. The summed output from the activity was recorded as a distribution line graph showing total activity collected over 1 min at any given point along the device. The summed area under the curve of this data then allowed for approximate assessment of total emission over the entirety of the device in addition to spatial distribution of ^{89}Zr labeled iron oxide.

2.11.1 Statistical analysis

Continuous flow: Statistical analysis was performed with statistics software (Stata SE 13.1, StataCorp, College Station, Texas). To determine the average count per minute (CPM) uptake difference between magnetized and non-magnetized devices, a linear mixed model was used with fixed effects for repeated sampling time, magnetization group, and the interactions between sampling time and magnetization group with random effects for repeated iterations of device testing. This method of analysis takes into account the correlation of repeated testing of the same device at each time-point. The main outcome measure, CPM uptake difference, was calculated as the difference between CPM sampled in open phosphate buffered saline (PBS) containing no device minus CPM sampled with the device present for each time-point (0, 1, 5, and 10 s). Linear marginal predictions were used after modeling to determine mean CPM uptake differences for magnetized devices and non-magnetized devices at each sampling time-point. Results are presented as β coefficients, which can be interpreted as the average difference in CPM uptake between device types per unit increase in sampling time. Marginal effects are plotted as average CPM difference per sampling time-point, with 95 % confidence intervals (CIs) for each device. β coefficients for pairwise comparisons are also interpreted as the average difference for CPM uptake between device types at each time point with corresponding p-values.

A linear mixed model was also used to determine which features of magnetic device significantly optimizes CPM uptake with fixed effects for diameter, length, orientation, sampling time and random effects for repeated iterations of each device. The relationship between diameter and CPM uptake modified by length, magnetic orientation, and CPM uptake modified by length, and diameter and CPM uptake modified by orientation were investigated by including two-way interactions in the model with sampling time as fixed effects and repeated iterations as random effects. Additionally, two-way interactions were included in a separate model for each magnetic device characteristic of diameter, length and

Author Manuscript Author Manuscript Author Manuscript Author Manuscript

orientation, and sampling time as fixed effects and repeated iterations as random effects to calculate predictive margins at each time-point. Marginal effects were used to determine the mean CPM uptake difference for each device characteristic for each time-point based on linear modeling. Results for main effects are presented as β coefficients, which can be interpreted as the average CPM uptake difference, controlling for time-point, against reference categories for each categorical variable: diameter, length, and orientation. Likewise, results for interactions are presented as β coefficients, which represent CPM uptake differences modified by a third variable.

In all the analyses, we considered differences statistically significant when the 2-tailed p-value was less than 0.05.

Multiple pass flow: For multiple pass experiments, the main outcome measure was CPM uptake, as baseline CPM with no device at each time-point was not recorded. The same linear mixed model approach was used to determine: i) Average CPM differences between magnetized *vs.* non-magnetized devices at each pass while incorporating random effects for testing iteration; ii) The main effects for device characteristics on CPM uptake while incorporating random effects for iteration; iii) Two-way interactions for device characteristics in CPM uptake with random effects; and iv) Two-way interactions for each device characteristic for each pass with random effects. CPM averages, standard deviations, and standard errors for continuous variables were calculated for each pass, collapsed over testing iteration. In all of the analyses, we defined significance to be when the 2-tailed *p*-value was less than 0.05.

3 Results

3.1 Computational flow assessment

Both “D” and “L” designs had similar flow around the magnets (Fig. 3a,b). However, magnets placed in the alternating “D” configuration demonstrated a different magnetic flux density than magnets placed in the alternating “L” configuration (Fig. 3c). While “D” devices generate a lower magnitude magnetic field around the device, the field is constant along the device, maximizing opportunity for capture. “L” devices generate a much stronger magnetic field at the ends of the magnets, but there is little to no strength in the middle of these magnets, causing particles to accumulate in clusters along the device (Fig. 3d).

Device designs with magnetization across the diameter (“D”) had higher percent capture than designs with magnetization across the length (“L”). Increasing outer diameter of magnets increased particle capture as follows: “D” designs, 3 mm: 12.8–13.6 %, 4 mm: 16.6–17.6 %, 5 mm: 21.8–22.8 %; “L” designs, 3 mm: 5.6–10 %, 4 mm: 9.4–15.8 %, 5 mm: 18.2–21.2 %. While varying magnet length and spacing of “D” designs had minimal effect, particle capture increased with shorter magnets and decreased spacing in “L” designs (Fig. 3e).

3.2 *In vitro* continuous flow testing in PBS

Overall, we tested nine magnetized devices once, and then we tested two non-magnetized devices three times at four time periods, sampling at 0, 1, 5 and 10 min. We assessed the

Author Manuscript Author Manuscript Author Manuscript Author Manuscript

changes in CPM difference for magnetized *vs.* non-magnetized devices with a linear mixed model and combined all magnetized devices, creating two groups, in order to find the average CPM difference for each sample time point. Results for this model are presented in Table 3. Pairwise comparisons show a significant difference in CPM uptake between device types (magnetized *vs.* non-magnetized) at time-points 1, 5, and 10 min.

A second linear mixed model was used to identify the association between device characteristics and CPM uptake. Data in this model were limited to only magnetized devices. Fixed effects for diameter, length, orientation and sampling time-point were used with a random intercept for test iteration. No interactions were included in the model. Results are listed in Table 5. While controlling for all other device characteristics and sampling time there was no significant difference in CPM uptake for increased diameter, magnet length, or change in magnetization orientation while controlling for other device factors. Further details of the analysis may be found in the statistical supplement.

In summary, maximal particle capture by all device designs displayed no significant difference at the end point of the 10-min flow model, with all magnetic devices capturing 95 % or more of the iron-oxide in solution. Particle capture did vary slightly during the first minute of flow, ranging from 47 to 87 % at 1 min. This variation was less at 2 min, when most devices demonstrated 87 to 93 % capture (Fig. 4).

On visual inspection of the devices, all variations of device design were coated with a thick layer of iron-oxide residue with notable increase in deposition along the first two magnets in series. Devices placed in the linear imager for spatial radio-tracer assessment showed an unequal distribution of ^{89}Zr along their length, with increased concentration at the first few magnets in series on each device; for example, accumulation of particle preferentially at the leading edge of flow interaction with the devices. Overall device capture of ^{89}Zr qualitatively matched computational predictions, with “D” devices demonstrating particle accumulation evenly along each magnet, whereas “L” devices demonstrated particle accumulation on either end of each magnet comprising the device.

3.3 *In vitro* testing – multiple pass serum flow model

Each device type was tested for CPM mean uptake at four pass-points with three iterations per device leading to 96 total observations. Linear mixed effects results are presented in Table 4. Interactions for CPM uptake differences between magnetic devices and non-magnetic devices were significant for each pass compared to baseline pass 0 as were pairwise comparisons at each time-point. Results for investigation of the association between device characteristics and CPM uptake are displayed in Table 6. No device characteristics showed statistically significant improvement in CPM uptake compared to baseline.

Overall, multiple pass serum flow model testing confirmed significant capture of iron oxide nanoparticles for all variations of magnetic intravascular device design. Again maximal solution particle capture by all device designs displayed no significant difference at the end point of three total passes across the magnetic filter. Results following a single pass over a magnetic device displayed minor variation, but total capture ranged from 62 to 82 % of total

Author Manuscript Author Manuscript Author Manuscript Author Manuscript

particles removed from solution. Final filtration efficacy after three passes ranged from 87 to 96 % particle capture in solution (Fig. 5). Non-magnetic control devices showed no significant change in solution iron particle concentration after three passes. Visual inspection of all magnetic devices again showed increased deposition of iron oxide along the first magnets in series for all design configurations, with accumulation pattern matching that predicted by computational simulation.

3.4 Simulated effect of dynamic tilting of device in intravascular flow

From *in vitro* testing of the device in the flow model, it was apparent that the device's axis does not remain centered in the vessel, often bending and tilting across the vessel. To further quantitatively explore the effects of magnet placement within the vessel, the following simulations were run: (a) eight 4 mm OD, 5 mm length magnets, magnetized across diameter, spaced 1 mm apart, centered axially along the vessel (b) the same magnets were designated to lay in a diagonal line across the vessel (c) these magnets were designated to have a 3D bend such that the 8 magnets ran from the bottom of the vessel to the top, with a right-left-right bend (Fig. 6). The first parallel configuration resulted in 23.2 % capture of the 1500 infused particles, while the tilted and bend configurations captured 26.6 and 30.0 % of infused particles respectively.

3.5 Optimizing device sizing for target vessel

While positioning of device within the vessel plays a significant role, we also explored the question of how large magnets would theoretically need to be before reaching a threshold of 90 % particle capture. Thus, for vessels with diameter 0.75, 1.0, 1.5, 2, 3, 5 mm, we simulated devices with 4 magnets, 5 mm length, 1 mm spacing, and a variety of ODs. From these results (Fig. 7), we can see that all particles could be captured with devices covering less than 50 % of the vessel diameter. Additionally, as the target vessel becomes smaller, a reduced cross sectional percentage of the vessel must be filled by a magnetic device to reach the ideal level of particle capture, as demonstrated by the minimum device outer diameter that predicts at least 90 % capture.

4 Discussion

In summary, the simulated model predicts that endovascular magnetic filters made from permanent N52 magnets demonstrate maximum particle capture when magnetized in the diameter ("D") configuration. This computational study predicts that endovascular magnetic filters made from permanent N52 magnets demonstrate maximum particle capture when magnetized in the "D" configuration. Additionally, efficacy of magnetic filter prototypes could be improved by using magnets with a larger outer diameter, providing increased magnetic field strength for capture. However, in both continuous and multiple pass *in vitro* flow models, while there was significant capture by all device designs as compared to the control non-magnetic devices, there was no significant difference in particle capture when the following parameters were varied: magnetization orientation, outer diameter (3, 4, 5 mm), magnet length (5, 10 mm), spacing (1, 3 mm).

Author Manuscript Author Manuscript Author Manuscript Author Manuscript

We found that our measurements were consistent with other published studies in the literature, with up to 90 % capture of particles from PBS and serum with a filtration device in place (Patel et al. 2014; Mabray et al. 2015). Many groups have been developing drugs conjugated to magnetic nanoparticles or loaded into magnetic microcapsules for targeted therapy delivery in cancer, inflammatory diseases, and more (Gautier et al. 2012; Chakkarapani et al. 2015; Mody et al. 2013). Furthermore, magnetic therapeutics have been tested in combination with intra-arterial delivery to liver tumors in rodent and rabbit animal models (Kim et al. 2015; Lee et al. 2013). These demonstrate a modern drug delivery paradigm that could benefit from the use of a filter downstream of infusion to further localize therapy to target regions. The high capture rates indicate that implementation of an intravascular magnetic filtration device may be feasible.

We noticed several trends that provide guidance for future construction of devices. First, we found that smaller devices were more flexible, thus crossing more laminar flow lines and allowing for similar capture to larger devices. Secondly, our computations demonstrated that there is an optimal maximal size of device that can still capture 90 % of particles infused into a given sized vessel. We observed that a larger device, which may occlude blood flow and promote clotting, could be foregone in favor of a smaller, more flexible device that captures more magnetic particles by crossing more laminar flow layers. Additionally, since increased length has little to no effect on increasing particle capture, shorter magnets may be used, enabling greater flexibility for interventional procedures with complex vasculature. In the future, computational simulations could be modeled for patient-specific anatomy based on medical images, to determine the minimum-size device that maximizes particle capture from flow, prior to treatment.

While this study was able to relate experimental and simulation, there were limitations. The simulated particle capture was significantly lower than we expected, possibly due to the lower number of magnets simulated as compared to the number in an experimental device (4 magnets *vs.* 14 magnets), a constraint that was imposed due to the extensive computation time with additional magnets. Additionally, the computational constraint that the device's axis remain centered within the vessel most likely reduced theoretical capture, since *in vitro* the device was shifting around the vessel, crossing more laminar flow lines than expected, thus increasing capture of particles. The experimental results of particle capture of 87–93 %, while adequately high, were surprising in that there was no significant difference between varied parameters. This may be because of limitations in sampling sensitivity, as only 3 mL of the entire flowing solution is characterized for concentration; while mixing prior to sampling was completed, the slight variances detected with computational simulation may not be captured as accurately with our *in vitro* quantification method. Characterization of particle capture on the device remains to be addressed; while overall distribution patterns could be characterized, quantification was inaccurate due to the asymmetric capture by "D" devices around a given magnet. Additional computational simulations indicate that other factors affect particle capture; for example, a flexible device that crosses multiple laminar flow layers within the vessel captures particles more effectively than one remaining centered within the vessel. Furthermore, the endovascular magnetic filter may be optimized based off of target vessel size. For a given vessel, there exists a target cross-sectional area coverage of device that results in maximal capture. Thus, our *in vitro* flow findings are consistent with

Author Manuscript Author Manuscript Author Manuscript Author Manuscript

these simulations: devices with smaller magnets were more flexible and were perturbed more in the flow model than devices with larger magnets, allowing for increased capture of magnetic nanoparticles. With regard to device construction, we have determined that a device with magnetization across the diameter and alternating polarity is the most promising design. Although these "D" devices did not perform significantly better in *in vitro* flow models than "L" devices, there is greater design safety due to less strain on the catheter, since the magnets are attracted to each other and spaced out as opposed to magnets repelling each other and forced together with clamps on either end.

In conclusion, the simulated model predicted that endovascular magnetic filters made from permanent N52 magnets demonstrate maximum particle capture when magnetized in the "D" configuration, with the device best practically optimized with shorter 5 mm magnets for flexibility and 1 mm spacing to preserve a consistent magnetic field. Computational simulation is a promising tool to evaluate efficacy of different designs of endovascular magnetic filters for capture of magnetic nanoparticle-conjugated chemotherapeutics.

Acknowledgments

Grant Support NIH 5R01EB012031 (SWH)

NIH 1R01CA194533 (SWH)

NIGMS MSTP T32GM007618 (SK)

NIH UL1 TR001872 (AC, MCM)

Radiology Departmental Seed Grant (MCM)

NIH R25EB013068 (SK, DL)

References

Brown, WF. Magnetic Materials. In: Condon, Odishaw, editor. Handbook of Chemistry and Physics. Vol. 8. McGraw-Hill; New York: 1958. Print

Cao Q, Han X, Li L. Numerical analysis of magnetic nanoparticle transport in microfluidic systems under the influence of permanent magnets. J Phys D: Appl Phys. 2012; 45:465001–465012.

Chakkarapani P, Subbiah L, Palanisamy S, et al. Encapsulation of methotrexate loaded magnetic microcapsules for magnetic drug targeting and controlled drug release. J Magn Magn Mater. 2015; 380:285–294.

Curley SA, Byrd DR, Newman RA, et al. Reduction of systemic drug exposure after hepatic arterial infusion of doxorubicin with complete hepatic venous isolation and extracorporeal chemofiltration. Surgery. 1993; 114:579–585. [PubMed: 8367814]

Curley SA, Newman RA, Dougherty TB, et al. Complete hepatic venous isolation and extracorporeal chemofiltration as treatment for human hepatocellular carcinoma: a phase I study. Ann Surg Oncol. 1994; 1:389–399. [PubMed: 7850540]

Driscoll C, Morris R, Senyei A. Magnetic targeting of microspheres in blood flow. Microvasc Res. 1984; 27(3):353–369. [PubMed: 6727704]

El-Sayed IH. Nanotechnology in head and neck cancer: the race is on. Curr Oncol Rep. 2010; 12:121–128. [PubMed: 20425597]

Fuhrman GM, Cromeens DM, Newman RA, et al. Hepatic arterial infusion of verapamil and doxorubicin with complete hepatic venous isolation and extracorporeal chemofiltration: pharmacological evaluation of reduction in systemic drug exposure and assessment of hepatic toxicity. Surg Oncol. 1994; 3:17–25. [PubMed: 8186867]

Author Manuscript Author Manuscript Author Manuscript Author Manuscript

Furlani EP, Ng KC. Analytical model of magnetic nanoparticle transport and capture in the microvasculature. Phys Rev E. 2006; 73(6):1–10.

Gautier J, Munnier E, Paillard A, et al. A pharmaceutical study of doxorubicin-loaded PEGylated nanoparticles for magnetic drug targeting. Int J Pharm. 2012; 423(1):16–25. [PubMed: 21703340]

Goodwin SC, Bittner CA, Peterson CL, Wong G. Single-dose toxicity study of hepatic intra-arterial infusion of doxorubicin coupled to a novel magnetically targeted drug carrier. Toxicol Sci. 2001; 60:177–183. [PubMed: 11222884]

Guskos N, Zolnierkiewicz G, Typek J, et al. Magnetic resonance study of ZnO-Fe_2O_3-$ZnFe_2O_4$ system. Rev Adv Mater Sci. 2010; 23:224–228.

Haverkort J, Kenjeres S, Kleijn C. Computational simulations of magnetic particle capture in arterial flows. Ann Biomed Eng. 2009; 37(12):2436–2448. [PubMed: 19760148]

Kim D, Chen J, Omary R, et al. MRI visible drug eluting magnetic microspheres for transcatheter intra-arterial delivery to liver tumors. Theranostics. 2015; 5(5):477–488. [PubMed: 25767615]

Lammer J, Malagari K, Vogl T, et al. Prospective randomized study of doxorubicin-eluting-bead embolization in the treatment of hepato-cellular carcinoma: results of the PRECISION V study. Cardiovasc Intervent Radiol. 2010; 33:41–52. [PubMed: 19908093]

Lee I, Ahn C, Cha E, et al. Improved drug targeting to liver tumors after intra-arterial delivery using superparamagnetic iron oxide and iodized oil, preclinical study in a rabbit model. Invest Radiol. 2013; 48(12):826–833. [PubMed: 23835597]

Lyer S, Tietze R, Jurgons R, et al. Visualisation of tumour regression after local chemotherapy with magnetic nanoparticles- a pilot study. Anticancer Res. 2010; 30:1553–1557. [PubMed: 20592340]

Mabray M, Lillaney P, Sze C, et al. In vitro capture of small ferrous particles with a magnetic filtration device designed for intravascular use with intraarterial chemotherapy: proof-of-concept study. J Vasc Interv Radiol. 2015; 27(3):426–432. [PubMed: 26706187]

Mahmoudi M, Shokrgozar MA, Simchi A, et al. Multiphysics flow modeling and in vitro toxicity of iron oxide nanoparticles coated with poly(vinyl alcohol). J Phys Chem C. 2009; 113:2322–2331.

Mody V, Cox A, Shah S, et al. Magnetic nanoparticle drug delivery systems for targeting tumor. Appl Nanosci. 2013; 4(4):385–392.

Patel AS, Saeed M, Yee EJ, et al. Development and validation of endovascular chemotherapy filter device for removing high-dose doxorubicin: preclinical study. J Med Device. 2014; 8:410081–410088.

Ratariu O, Strachan N. Modelling magnetic carrier particle targeting in the tumor microvasculature for cancer treatment. J Magn Magn Mater. 2005; 293(1):639–646.

Sharma S, Katiyar VK, Singh U. Mathematical modelling for trajectories of magnetic nanoparticles in a blood vessel under magnetic field. J Magn Magn Mater. 2015; 379:102–107.

Song MJ, Chun HJ, do Song S, et al. Comparative study between doxorubicin-eluting beads and conventional transarterial chemoembolization for treatment of hepatocellular carcinoma. J Hepatol. 2012; 57:1244–1250. [PubMed: 22824821]

Wexler L, Bergel DH, Gabe IT, et al. Velocity of blood flow in normal human venae cavae. Circ Res. 1968; 23(3):349–359. [PubMed: 5676450]

Wilson MW, Kerlan RK Jr, Fidelman NA, et al. Hepatocellular carcinoma: regional therapy with a magnetic targeted carrier bound to doxorubicin in a dual MR imaging/conventional angiography suite -initial experience with four patients. Radiology. 2004; 230:287–293. [PubMed: 14695402]

Author Manuscript Author Manuscript Author Manuscript Author Manuscript

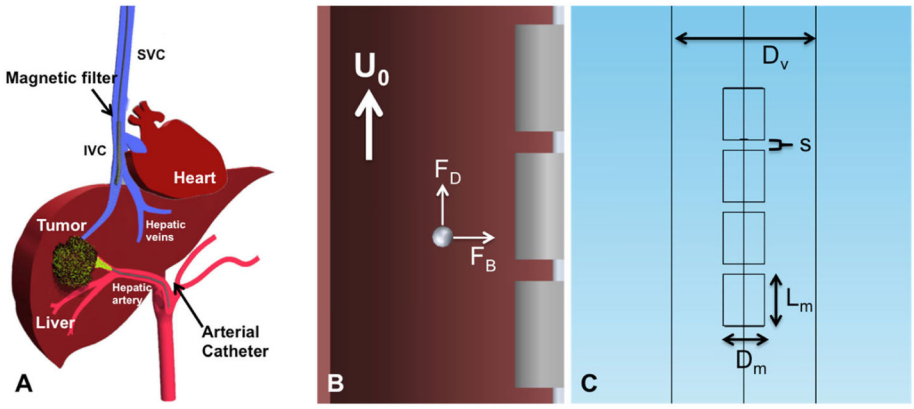

Fig. 1.

Schematic of endovascular magnetic filtration of nanoparticle-conjugated chemotherapy. **a** The magnetic chemofilter would be deployed in the inferior vena cava, downstream of intra-arterial infusion of chemotherapy. This would minimize therapy that reaches the heart and circulates systemically, causing toxic side effects. **b** Physical principles of capture: Drag forces pull the magnetic nanoparticles forward in flow, while the magnetic force from the N52 magnets pulls the particles towards the filter. **c** Parameters varied for device optimization were outer diameter and length of individual magnets, spacing between magnets, and magnetization orientation (not shown)

Author Manuscript Author Manuscript Author Manuscript Author Manuscript

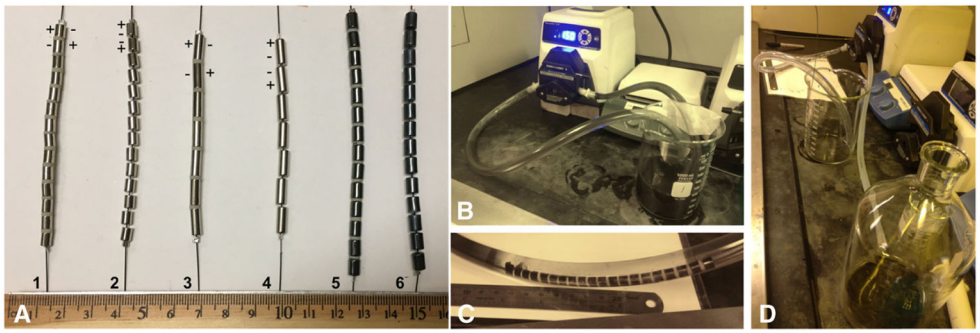

Fig. 2.

Prototype devices and flow model setups. **a** A representative sample of the intravascular magnetic chemofilters were tested in benchtop flow models: *1*) magnetization across diameter with alternating orientation ("D"), 4 mm outer diameter (OD), 5 mm length, 1 mm rubber spacers. *2*) magnetization along length with alternating orientation ("L"), 4 mm OD, 5 mm length, 1 mm spacing. *3*) "D" magnetization, 4 mm OD, 10 mm length, 1 mm rubber spacers. *4*) "L" magnetization, 4 mm OD, 10 mm length, 1 mm spacing. *5*) Control "D" device: no magnetization, 5.3 mm OD, 6 mm length, 1 mm rubber spacers. *6*) Control "L" device: no magnetization, 5.3 mm OD, 6 mm length, 1 mm spacing. **b** The continuous flow benchtop setup utilized a single 1 L reservoir with 500 mL solution circulating past device. C) Device in tubing, with flow going from left to right. **d** The multiple pass flow benchtop setup used two 1 L reservoirs, with 500 mL solution passing from initial reservoir to final reservoir, where a concentration sample after each full pass is taken

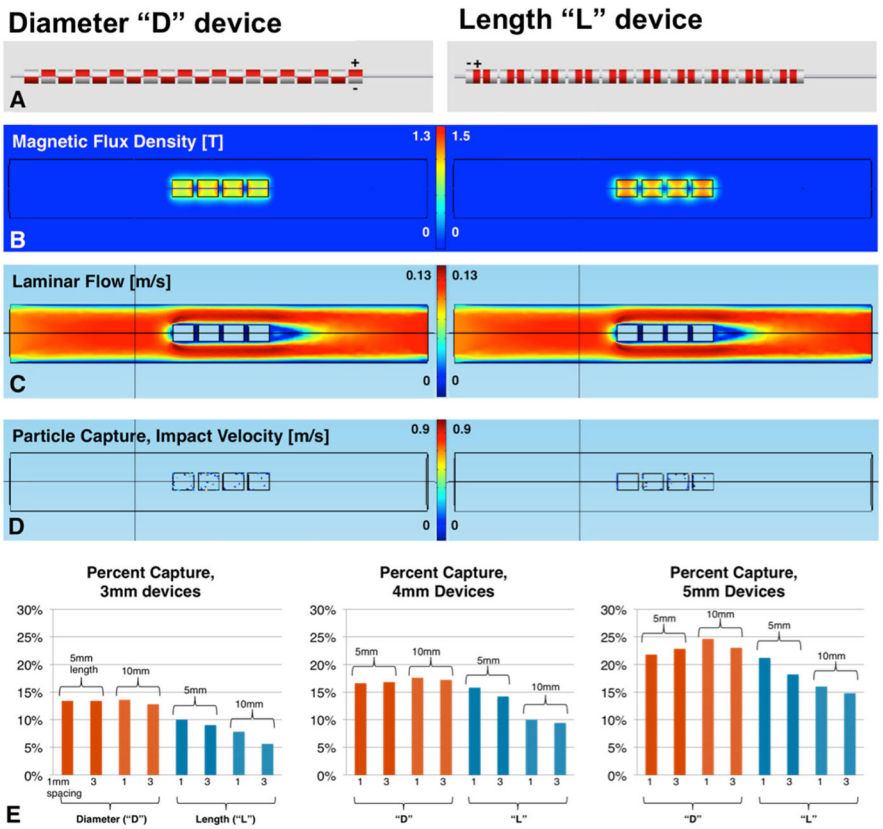

Fig. 3.

Summary of computational particle capture results. **a** Left, CAD image of "D" magnetization device; Right, CAD image of "L" magnetization device. **b** Magnetic flux density generated by 4 mm OD, 5 mm length, 1 mm spacing device of each corresponding magnetization orientation. Four magnets are simulated to minimize computation time. **c** Laminar flow is demonstrated to be similar around each device given identical dimensions. **d** Left, particle capture occurs evenly across the surface of each magnet, as predicted by the uniform surface magnetic flux density of the "D" magnetization device. Right, particle capture mostly occurs at either end of each magnet, as predicted by the greater magnetic flux density at magnet ends of the "L" magnetization device. **e** Percent of particles captured by each device from a 1500 particle infusion. L-R: increasing device diameter, holding vessel diameter constant. *Red bars* indicate capture by devices with "D" magnetization, and *blue bars* indicate capture by devices with "L" magnetization. "D" devices are predicted to have slightly greater capture, with varying length having minimal effect

Author Manuscript Author Manuscript Author Manuscript Author Manuscript

Author Manuscript Author Manuscript Author Manuscript Author Manuscript

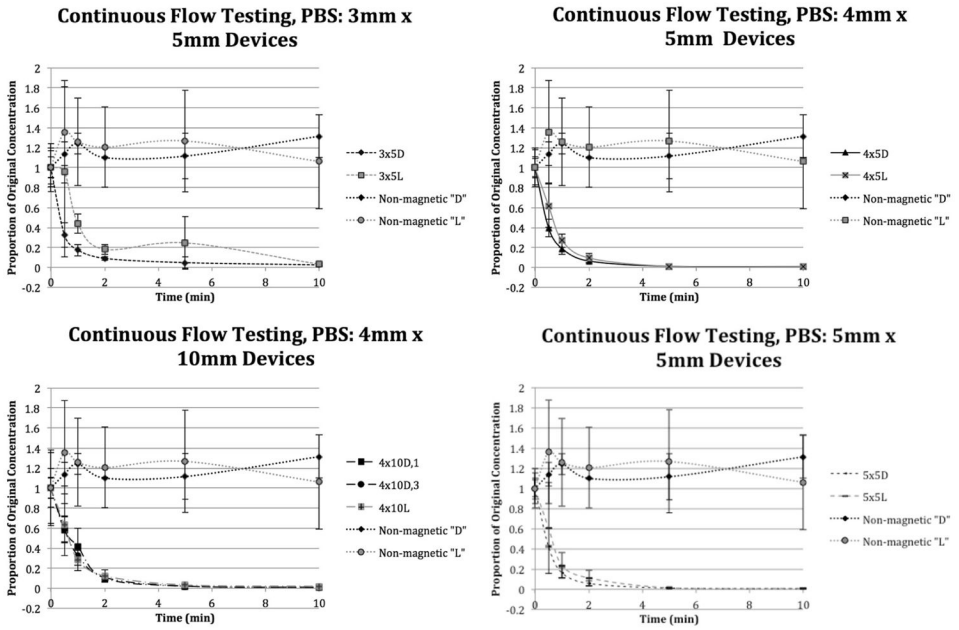

Fig. 4.

Continuous flow testing results. *Top left*: 3 mm OD, 5 mm length devices; there is significant particle capture by magnetic devices as compared to control; however there was little difference between “D” magnetized and “L” magnetized devices. *Top right*: 4 mm OD, 5 mm length devices; there is significant particle capture by magnetic devices as compared to control; however there was little difference between “D” magnetized and “L” magnetized devices. *Bottom left*: 4 mm OD, 10 mm length devices; there is significant particle capture by magnetic devices as compared to control; however there was little difference between “D” magnetized and “L” magnetized devices, and between 1 mm and 3 mm spacing. *Bottom right*: 5 mm OD, 5 mm length devices; there is significant particle capture by magnetic devices as compared to control; however there was little difference between “D” magnetized and “L” magnetized devices. In all cases, magnetic devices reduced initial particle concentration by 80–90 % within 2 min

Author Manuscript Author Manuscript Author Manuscript Author Manuscript

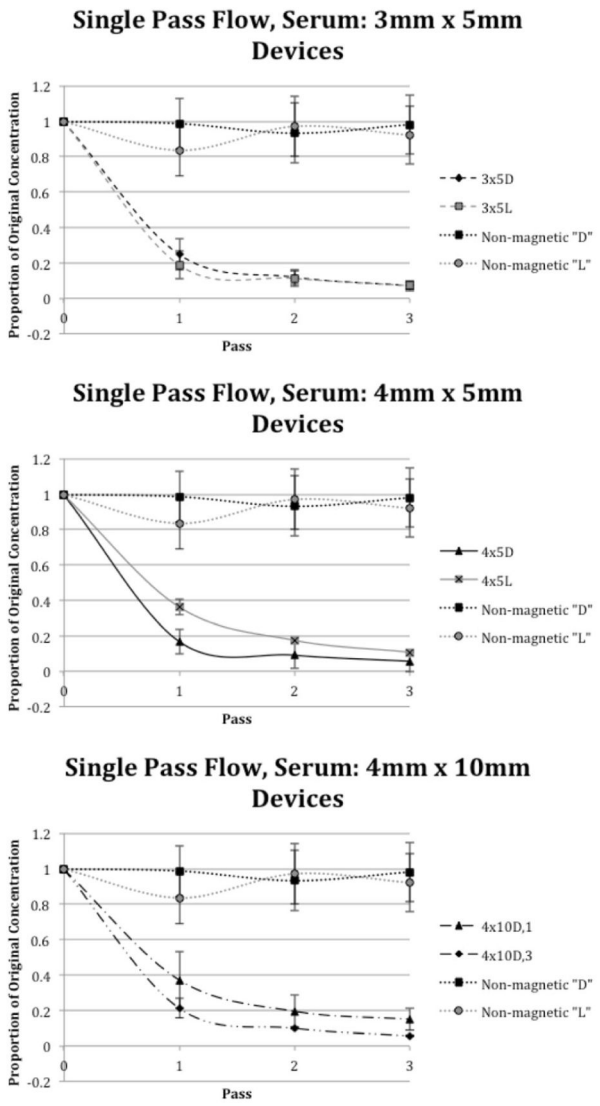

Fig. 5.

Multiple pass flow testing results. *Top*: 3 mm OD, 5 mm length devices; there is significant particle capture by magnetic devices as compared to control; however there was little difference between "D" magnetized and "L" magnetized devices. *Middle*: 4 mm OD, 5 mm length devices; there is significant particle capture by magnetic devices as compared to control; there is greater capture by the "D" device at the single pass mark, but little difference between "D" magnetized and "L" magnetized devices after the second and third pass. *Bottom*: 4 mm OD, 10 mm length devices; there is significant particle capture by magnetic devices as compared to control; however there was little difference between 1 mm and 3 mm spacing

Author Manuscript Author Manuscript Author Manuscript Author Manuscript

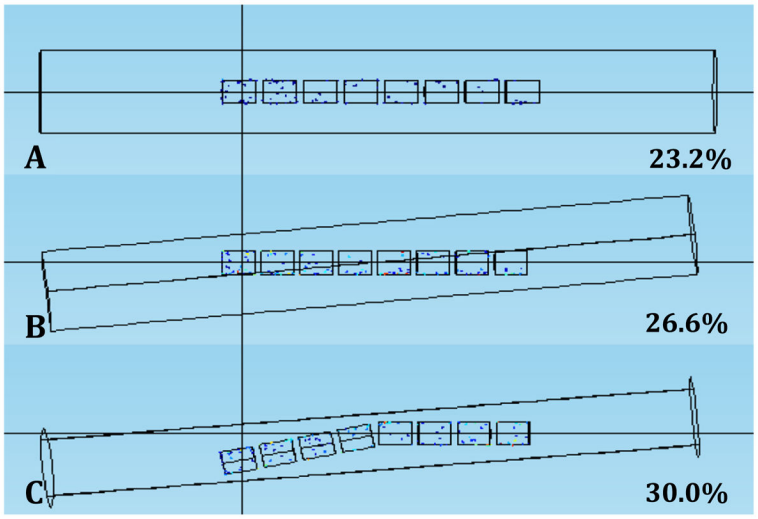

Fig. 6.

Simulated effect of tilting the device within the vessel. **a** Particle capture by 8 magnets in "D" configuration, 4 mm OD, 5 mm length, 1 mm spacing, centered within the vessel. **b** Particle capture by magnets that are still in a straight line, but now tilted within the vessel to cross more laminar flow lines and encounter more particles. **c** Particle capture by magnets in a "3D bend" configuration. This bend is tilted into the page as well, increasing the amount of flow that the device encounters, resulting in 29 % greater capture than in (**a**)

Author Manuscript Author Manuscript Author Manuscript Author Manuscript

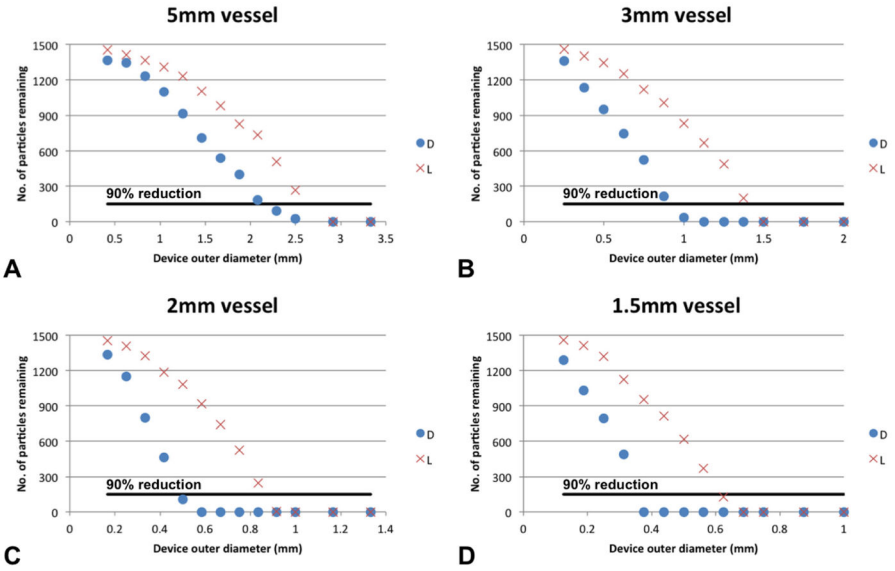

Fig. 7.

Simulated particle capture *vs.* magnetic device diameter. **a**–**d** Decreasing vessel sizes, with corresponding smaller device capture results. Black line indicates 90 % capture of 1500 particle infusion. “D” devices exhibit a greater exponential rise to maximum capture than “L” devices across each of the vessel sizes. As vessel diameter decreases, relative diameter of device to vessel necessary for maximum capture also decreases (exhibited by curve shift to the left)

Author Manuscript Author Manuscript Author Manuscript Author Manuscript

Table 1

Summary of device COMSOL simulations

Device:	3x5L	3x5D	3x10L	3x10D	4x5L	4x5D	4x10L	4x10D	5x5L	5x5D	5x10L	5x10D
Mag: Length	X		X		X		X		X		X	
Mag: Diameter		X		X		X		X		X		X
OD: 3 mm	X	X	X	X								
OD: 4 mm					X	X	X	X				
OD: 5 mm									X	X	X	X
Length: 5 mm	X	X			X	X			X	X		
Length: 10 mm			X	X			X	X			X	X
Spacing (mm)	1,3	1,3	1,3	1,3	1,3	1,3	1,3	1,3	1,3	1,3	1,3	1,3
# Magnets	4,4	4,4	2,2	2,2	4,4	4,4	2,2	2,2	4,4	4,4	2,2	2,2

Convention: outer diameter (mm) × length of individual magnet (mm) + magnetization direction

Author Manuscript Author Manuscript Author Manuscript Author Manuscript

Table 2

Summary of prototype devices built for *in vitro* flow testing

Device:	3x5L	3x5D	4x5L	4x5D	4x10L	4x10D	5x5L	5x5D	N-M "L"	N-M "D"
Mag: Length	X		X		X		X		X	
Mag: Diameter		X		X		X		X		X
OD: 3 mm	X	X								
OD: 4 mm			X	X	X	X			X	X
OD: 5 mm							X	X		
Length: 5 mm							X	X	X	X
Length: 10 mm					X	X				
Spacing (mm)	1	1	1	1	1	1,3	1	1	1	1
# Magnets	14	14	14	14	7	7	14	14	14	14

Convention: outer diameter (mm) × length of individual magnet (mm) + magnetization direction

Author Manuscript Author Manuscript Author Manuscript Author Manuscript

Table 3

Association between magnetization and CPM difference over time, continuous flow

Device	Time	Margin of error	95 % CI of CPM difference	*P*
Non-Magnetic (NM)	All	−0.440	−86.304–−85.424	0.992
Magnetic (M)	All	207.897	167.609–248.184	$p < 0.001$*
NM	0	40.530	−131.184–212.244	.644
NM	1	−25.671	−197.385–146.043	.770
NM	5	−5.789	−177.503–165.925	.947
NM	10	−12.071	−183.785–159.643	.890
M	0	−3.424	−82.9117–76.065	.933
M	1	216.454	135.508–297.401	$p < 0.001$*
M	5	301.845	220.898–382.791	$p < 0.001$*
M	10	323.115	242.168–404.061	$p < 0.001$*

Author Manuscript

Author Manuscript

Author Manuscript

Author Manuscript

Table 4

Association between magnetization and CPM difference each pass, multiple pass flow

Device	Time	Margin of error	95 % CI of CPM difference	*P*
Non-Magnetic (NM)	All	144.933	85.200–204.630	$p < 0.001$*
Magnetic (M)	All	176.009	141.543–210.475	$p < 0.001$*
NM	0	155.653	36.259–275.457	0.011
NM	1	136.915	17.521–256.308	0.025
NM	2	145.045	25.652–264.438	0.017
NM	3	142.123	22.730–261.516	0.020
M	0	517.721	448.790–586.653	0
M	1	104.708	35.777–173.640	0.003
M	2	50.610	−18.321–119.542	0.150
M	3	30.997	−37.935–99.928	0.378

Author Manuscript Author Manuscript Author Manuscript Author Manuscript

Table 5

Association between device characteristics and CPM difference over time, continuous flow

Independent Variable	**β coefficient**	**95 % CI of CPM difference**	***P***
Diameter (Base = 3 mm)			
4 mm	35.437	−95.507–166.381	0.596
5 mm	22.575	−108.369–153.519	0.735
Length (Base = 5 mm)			
10 mm	9.552	−112.071–131.174	0.878
Orientation (Base = D)			
L	48.349	−41.080–137.778	0.289
Sampling Time Point (Base = 0)			
1 min	218.115	94.525–341.704	0.001
5 min	303.505	179.915–427.095	
10 min	324.775	201.185–448.365	
Random-Effects Parameters	Estimate	95 % CI	*P*
Testing Iteration	4.230E-17 5.460E + 04	1.860E-24–9.660E-10 41881.220–71223.290	1.000 1.000

Author Manuscript Author Manuscript Author Manuscript Author Manuscript

Table 6

Association between device characteristics and CPM difference each pass, multiple pass flow

Independent Variable	**β coefficient**	**95 % CI of CPM difference**	***P***
Diameter (Base = 3 mm)			
4 mm	36.017	−59.268–131.302	0.459
Length (Base = 5 mm)			
10 mm	−79.803	−186.335–26.729	0.708
Orientation (Base = D)			
L	−18.181	−113.466–77.10362	0.708
Sampling Pass (Base = 0)			
Pass 1	−413.013	−523.039–−302.988	$p < 0.001$
Pass 2	−467.111	−577.136–−357.086	$p < 0.001$
Pass 3	−486.725	−596.750–−376.700	$p < 0.001$
Random-Effects Parameters	Estimate	95 % CI of CPM difference	*P*
Testing Iteration – Constant	272.245	0.0468–1582551.0	0.400
Testing Iteration – Residual	28361.720	20314.910–39595.880	0.400